

Layer-Specific Functional and Anatomical MRI of the Retina With Passband Balanced SSFP

Eric R. Muir^{1–4} and Timothy Q. Duong^{1–3,5*}

The retina consists of multiple cellular and synaptic layers and is nourished by two distinct (retinal and choroidal) circulations bounding the retina, separated by an avascular layer. High spatiotemporal resolution, layer-specific MRI of the retina remains challenging due to magnetic inhomogeneity-induced artifacts. This study reports passband balanced steady-state free-precession (bSSFP) MRI at $45 \times 45 \times 500 \mu\text{m}$ and 1.6 s temporal resolution to image the mouse retina, overcoming geometric distortion and signal dropout while maintaining rapid acquisition and high signal-to-noise ratio. bSSFP images revealed multiple alternating dark-bright-dark-bright retinal layers. Hypoxic (10% O_2) inhalation decreased bSSFP signals in the two layers bounding the retina, corresponding to the retinal and choroidal vasculatures. The layer in between showed no substantial response and was assigned the avascular photoreceptor layers. Choroidal responses ($-25.9 \pm 6.4\%$, mean \pm SD, $n=6$) were significantly ($P < 0.05$) larger than retinal vascular responses ($-11.6 \pm 2.4\%$). bSSFP offers very high spatiotemporal resolution and could have important applications in imaging layer-specific changes in retinal diseases. Magn Reson Med 66:1416–1421, 2011. © 2011 Wiley Periodicals, Inc.

Key words: steady state free precession; SSFP; fMRI; retina; ophthalmology; hypoxia

INTRODUCTION

The retina consists of multiple structured layers. Starting from the vitreous, anatomical layers of the neural retina are the nerve fiber layer/ganglion cell layer, inner plexiform layer, inner nuclear layer, outer plexiform layer, outer nuclear layer, and inner and outer segments. The retina is nourished by two separate blood supplies: the retinal and choroidal circulations (1). Retinal vessels are mainly localized on the inner surface of the retina, with arterioles and capillaries projected into the ganglion cell layer, inner

plexiform layer, and inner nuclear layer. The choroidal vessels are located external to the neural retina, separated from the photoreceptor segments by the retinal pigment epithelium. The outer nuclear layer and the inner and outer segments, located in between the retinal and choroidal vascular layers, are avascular. The neural retina and choroid together are about $270 \mu\text{m}$ thick in rodents (2). Choroidal blood flow is many times greater than retinal blood flow (1,3,4), and the two vasculatures are regulated differently (5). Some retinal diseases affect the two circulations differently (6). The ability to noninvasively image layer-specific anatomy and “evoked” responses in the retina with depth resolution could have the potential to provide important clinically relevant information (7).

Layer-specific structural MRI has been reported in rats (2), cats (8), and mice (9). Relaxation times and apparent diffusion coefficient have been reported in rats (10), cats (8), and mice (9). Three to four layers were detected. MRI after intraperitoneal manganese-chloride injection showed three layers in the rodent retina (11,12) and MRI after intraocular manganese-chloride injection revealed seven distinct bands of alternating hyper- and hypointensities in rat retinas (13).

Blood-oxygenation-level-dependent (BOLD) fMRI of the retina associated with physiologic stimulations (2) and visual stimulation (14) has been reported using echo-planar-imaging (EPI). Blood flow fMRI with EPI readout has also detected changes due to physiologic stimulations in the retina (15). BOLD fMRI (2) and blood flow fMRI (16) responses to physiological challenges are perturbed in rodent models of retinal degeneration.

Most BOLD fMRI studies utilize EPI readout for rapid image acquisition, but EPI is prone to susceptibility artifacts such as geometric distortion and signal dropout. The retina is susceptible to these artifacts because the eye is located in a region with substantial magnetic inhomogeneity. Balanced steady state free precession (bSSFP) sequences have been proposed to achieve fast acquisition and high signal-to-noise ratio, while avoiding geometric distortion and signal dropout artifacts. bSSFP is, however, sensitive to off-resonance frequency shifts which result in passbands with high signal intensity and transition bands with low signal intensity on the images (17,18). Passband bSSFP fMRI which uses the wider and more stable passband region (17) was recently demonstrated in the human brain (19). Although its signal sources is not fully understood (17–20), passband bSSFP fMRI has similar oxygen-dependent signal changes as T_2 or T_2^* BOLD fMRI, depending on TR/TE and field strength (20).

¹Department of Ophthalmology, Research Imaging Institute, University of Texas Health Science Center, San Antonio, Texas, USA.

²Department of Radiology, Research Imaging Institute, University of Texas Health Science Center, San Antonio, Texas, USA.

³Department of Physiology, Research Imaging Institute, University of Texas Health Science Center, San Antonio, Texas, USA.

⁴Department of Biomedical Engineering, Georgia Institute of Technology, Atlanta, Georgia, USA.

⁵South Texas Veterans Health Care System, San Antonio, Texas, USA.

Grant sponsor: National Eye Institute/National Institutes of Health; Grant numbers: R01 EY018855, R01 EY014211; Grant sponsor: Department of Veterans Affairs (VA MERIT Award).

*Correspondence to: Timothy Q. Duong, Ph.D., Research Imaging Institute, UTHSCSA, 8403 Floyd Curl Dr, San Antonio, TX 78229. E-mail: duongt@uthscsa.edu

Received 15 December 2010; revised 23 February 2011; accepted 7 March 2011.

DOI 10.1002/mrm.22935

Published online 20 May 2011 in Wiley Online Library (wileyonlinelibrary.com).

The purpose of this study was to explore the feasibility of passband bSSFP fMRI to resolve layer-specific changes in the mouse retina at $45 \times 45 \times 500 \mu\text{m}$ and 7 T. As a demonstration, hypoxic challenge was used to modulate the bSSFP signals. Passband bSSFP fMRI provided images of the retina with high spatiotemporal resolution, sensitive to blood oxygenation changes, and free of geometric distortion and dropout artifacts, overcoming some limitations of EPI-based fMRI previously reported in the rodent retina (2).

MATERIALS AND METHODS

Animal Preparation

Normal male C57BL/6 mice (8–16 weeks old, ~ 25 g, $n=6$) were studied with institutional approval and in accordance with the Statement for the Use of Animals in Ophthalmic and Vision Research. Animals were first anesthetized with 5% isoflurane, put into a head holder with ear and tooth bars, and placed in an animal cradle with a circulating warm water pad and nose cone for anesthesia and gas delivery. Imaging was performed under 1.1% isoflurane and spontaneous breathing conditions. Mice were provided 30% O_2 in N_2 as the baseline condition. The hypoxic challenge involved 4.7 min of baseline and 4.7 min of hypoxia (10% O_2) and was repeated twice with 10 min rests between trials. Respiration rate, heart rate, oxygen saturation, and rectal temperature were monitored, and temperature was maintained at $37 \pm 0.5^\circ\text{C}$.

MRI Methods

MRI was performed on a 7-T/30-cm magnet with a 150 G/cm BGA6S gradient insert (Bruker, Billerica, MA). A small circular surface eye coil (ID = 0.6 cm) was placed over the left eye. A coronal slice bisecting the optic nerve head was obtained with bSSFP. Parameters were FOV = 5×5 mm, matrix = 112×112 ($45 \times 45 \mu\text{m}$), bandwidth = 30 kHz, one 0.5 mm thick slice, and TE/TR = 3.67/7.34 ms. Data were oversampled by a factor of 2 in the frequency and phase encode directions, effectively doubling the FOV and matrix, to improve signal-to-noise ratio and avoid aliasing (the acquisition time was doubled compared to nonoversampled acquisition). Two averages were acquired in k -space per time point giving 3.3 s temporal resolution per image. FASTMAP (fast automatic shimming technique by mapping along projections) shimming (21) was used to minimize banding, and the RF phase cycling was adjusted to move bands away from the retina. Alternatively, bSSFP images were acquired with four alternating RF phase cycling angles (0, 90, 180, and 270°) and combined to remove banding ($n = 1$). For comparison, EPI was acquired with FOV = 6×6 mm, matrix = 134×134 ($45 \times 45 \mu\text{m}$), two segments, bandwidth = 333 kHz, one 0.5 mm thick slice, TE = 12.0 ms, TR = 2000 ms per segment, and with a 3/4 partial Fourier acquisition in the phase encode direction.

Data Analysis

bSSFP images were zero-padded to 128×128 and EPI images to 153×153 (nominal resolution of $39 \times 39 \mu\text{m}$ for

both). bSSFP images acquired with four phase cycling angles were combined using the nonlinear averaging method (22), in which the three-highest intensities from the four magnitude images are averaged, before co-registration. The nonlinear averaging method has been shown to provide good signal-to-noise ratio and suppression of transition bands, is simple to implement, and requires only the magnitude data (22,23). Time-series images were first aligned using the spatial realignment function in the Statistical Parametric Mapping software, and further aligned and analyzed using custom-written codes written in Matlab (Math-Works, Natick, MA) as detailed below.

First, the retina was linearized by taking image intensity profiles across the retinal thickness by projecting lines perpendicular to the vitreous-retina boundary, found using edge-detection (2). Profiles were obtained at $4 \times$ spatial interpolation in the direction perpendicular to the retina. Further time-series co-registration was performed on the linearized profiles in Matlab. This was done by correcting for one dimensional translation in the direction perpendicular to the retina. This time-series realignment was first done on the entire linearized retina to correct global motion of retina. Then, to correct for motion locally, the linearized retina was spatially divided into small equally-sized segments in the direction parallel to the retina (Fig. 2). The time-series realignment was then applied individually to each small segment of the retina. The time-averaged %-change between baseline and hypoxia was calculated for the linearized retina, and this %-change map was then spatially averaged along the length of the retina. Peak %-change values were then determined from the final averaged %-change profile for each animal.

The co-registered profiles were reconstructed back onto images for display and calculation of %-change maps. Percent changes maps were calculated using STIMULATE (University of Minnesota) software with a 95 or 99% confidence interval, a %-change threshold from -5 or -7% to -100% and a cluster size of at least 20 contiguous pixels. The %-change map was masked around the transition bands in the anterior portion of the eye. Group-average data were tabulated and expressed as mean \pm standard deviation (SD). Statistical analysis used two-sided t -tests with $P < 0.05$ indicating statistical significance.

RESULTS

Under 30% O_2 (baseline), the respiration rate was 91 ± 11 breaths/min, heart rate was 371 ± 29 beats/min, and oxygen saturation was $97 \pm 1\%$. Under 10% O_2 , the respiration rate was 106 ± 11 breaths/min, heart rate was 453 ± 65 beats/min, and oxygen saturation was $68 \pm 6\%$, all statistically different from baseline ($P < 0.01$).

Representative EPI and bSSFP images of the same eye are shown in Fig. 1. EPI shows obvious distortion in the retina as well as the rest of the eye. One to three distinguishable retinal layers were usually detected in EPI. In contrast, bSSFP produced images free of image distortion and signal dropout. bSSFP images showed four distinguishable dark-bright-dark-bright retinal layers along the entire retina.

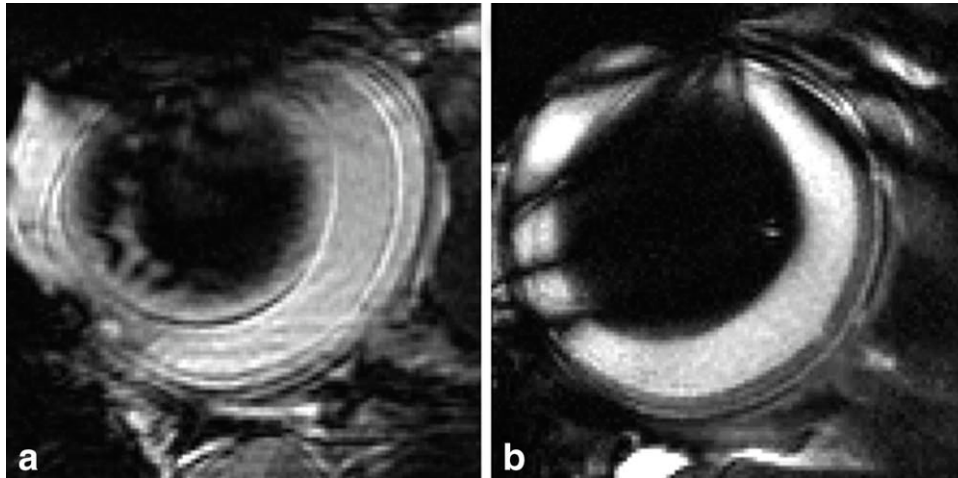


FIG. 1. **a:** EPI image ($45 \times 45 \times 500 \mu\text{m}$) demonstrating artifacts in the eye. Phase encoding orientation is left-right. **b:** bSSFP image ($45 \times 45 \times 500 \mu\text{m}$) from the same animal acquired during baseline conditions has clear retinal layers without distortion.

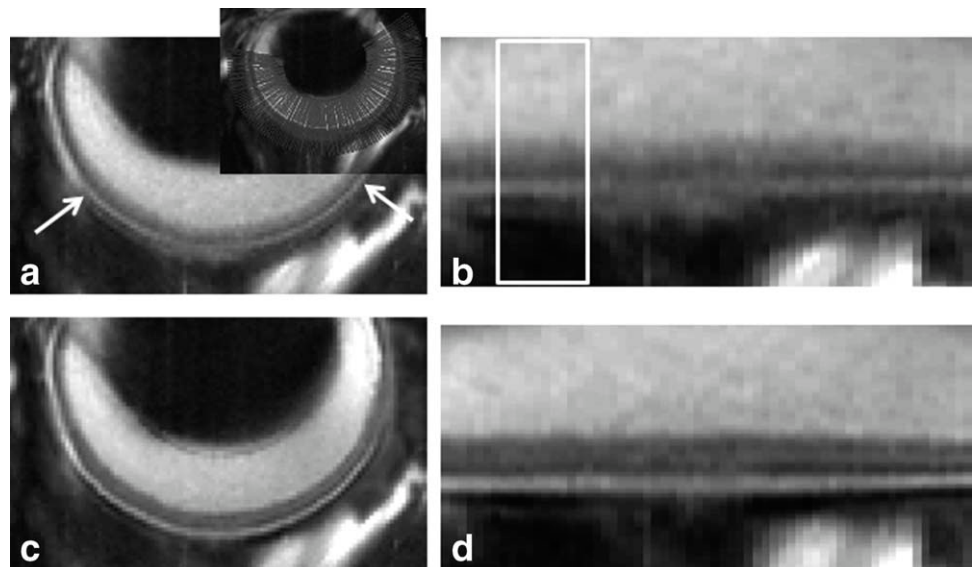
Figure 2 illustrates the alignment analysis protocol. The results of whole-image co-registration using Statistical Parametric Mapping and the corresponding linearized retina are shown in Fig. 2a,b. The results of additional profile co-registration on the linearized retina and on the reconstructed image are shown in Fig. 2c,d. There was a marked improvement in image quality with the additional profile co-registration in animals in which apparent motion occurred.

Figure 3a shows a representative %-change map associated with hypoxic challenge using bSSFP, demonstrating bSSFP signal decreases. Anatomy profiles during baseline and hypoxia depicted four alternating dark-bright-dark-bright layers (Fig. 3b). The %-change profiles and maps associated with hypoxic challenge had two well-resolved layers with functional response (Fig. 3c). These layers were assigned to be the retinal and choroidal vascular layers. A middle layer between these two vascular layers showed little change and was assigned as the avascular outer nuclear layer and inner and outer segments (photoreceptors). The group-averaged

%-changes were $-11.6 \pm 2.4\%$ in the inner (retinal) layer ($n = 6$, $P < 1 \text{ E}^{-4}$ one-sample *t*-test comparing the sample mean with zero), $-1.6 \pm 1.4\%$ in the middle (avascular) layer ($P < 0.05$), and $-25.9 \pm 6.4\%$ in the outer (choroid) layer ($p < 5\text{E-}4$). The inner and outer layer %-changes were statistically different ($P < 5\text{E-}3$). The middle layer %-change was statistically different from the inner ($P < 5\text{E-}4$) and outer layer ($P < 5\text{E-}4$). Figure 4 demonstrates that acquisition of four RF phase cycling angles can be used to remove all dark bands from the bSSFP image of the eye. The %-changes were -8.6% in the inner layer and -16.4% in the outer layer ($n = 1$).

The outermost hyperintense bSSFP anatomical layer lined up with the %-change peak of the choroid. The inner hypointense and hyperintense anatomical layers lined up with the %-change peak of the retinal layer and were assigned as the ganglion cell, inner plexiform and inner nuclear layers. The hypointense anatomical layer in the middle with the weak hypoxic response was assigned the avascular outer nuclear layer and inner and outer segments.

FIG. 2. **a:** Averaged image after rigid body motion correction. (Inset) bSSFP image showing profiles perpendicular to the vitreous-retinal edge. The white arrows indicate the region selected for profile analysis. **b:** The corresponding linearized retina. The white box indicates a segment of the retina consisting of 10 profiles. **c:** The reconstructed image with the realigned profiles. **d:** The linearized retina after the profile realignment. All images are the averaged time-series. [Color figure can be viewed in the online issue, which is available at wileyonlinelibrary.com.]



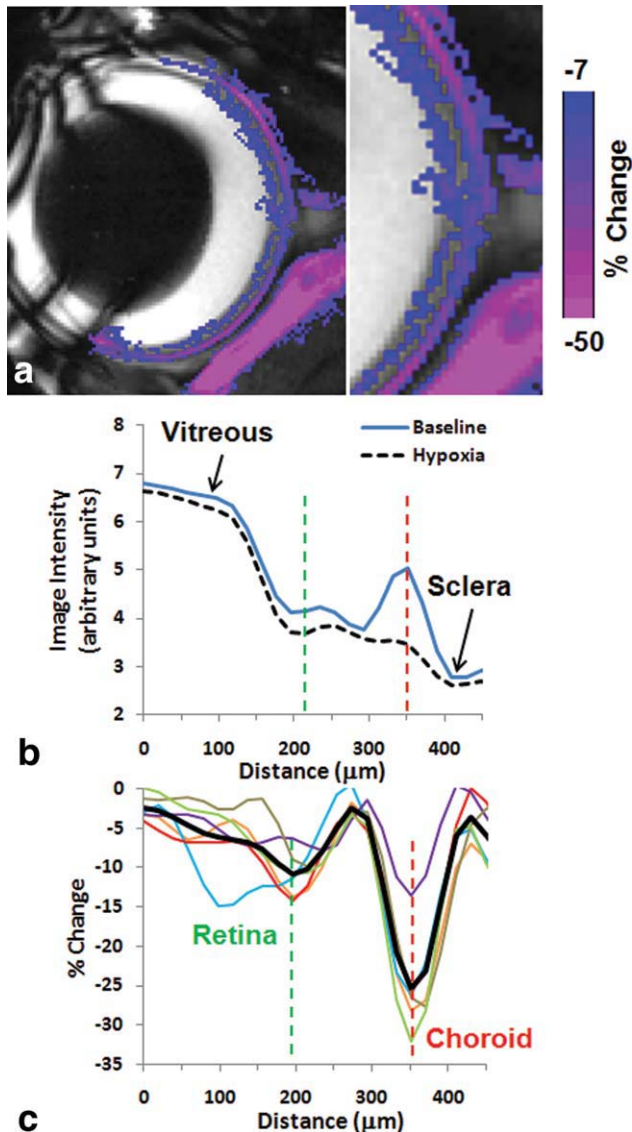


FIG. 3. **a**: Percent-change map in response to hypoxia from a single mouse at $45 \times 45 \times 500 \mu\text{m}$ overlaid on the bSSFP image. A 99% confidence interval was used with a %-change threshold of -7 to -100% . **b**: The corresponding anatomical intensity profiles (arbitrary units) of the retina during baseline and hypoxia. **c**: Percent-change profiles due to hypoxia from all animals ($n=6$). The thick black line is the group-averaged profile. The vertical red and green dashed lines indicate the peak choroidal and retinal vessel changes, respectively.

DISCUSSION

This study demonstrates high spatiotemporal resolution passband bSSFP fMRI of the retina free of magnetic susceptibility-induced signal drop out and geometric distortion. bSSFP detects multiple well-defined anatomical layers, is sensitive to blood-oxygenation changes, and detects layer-specific responses to hypoxic challenge in the retinal and choroidal vasculature, separated by the avascular region. The advantages of bSSFP fMRI are: high signal-to-noise ratio per unit time, similar temporal resolution to EPI, high spatial resolution, and improved image clarity compared with EPI. A potential problem

with bSSFP fMRI is banding artifacts, but the bands could be moved away from the region of interest by changing the RF phase cycling angle or could be removed using multiple RF phase cycling angles.

In contrast to previous studies of the rat retina which needed paralytics in addition to isoflurane (2,24), eye movement in isoflurane-anesthetized mice was found to be considerably less, so paralytics were not as necessary. This is fortunate because intubation, mechanical ventilation and paralysis, and recovery from paralysis are not trivial in mice. The difference in eye movement between mice and rats could be due to species difference or simply animal size. Nonuniform movements of the eye and retina rendered global rigid-body motion correction less effective. Profile realignment of the linearized retina effectively corrected the small subtle motions of the retina. With the improved spatial resolution of bSSFP and the detection of well resolved layers, this additional alignment step was important.

Because fMRI signal changes are generally small, image alignment of time-series fMRI data could potentially have unintended results, such as false activations or masking true activations. This is unlikely to be case here because the percent changes are large. It is nonetheless important to first minimize motion by improving animal setup and by using paralytics or other anesthetics (24), rather than to rely on postprocessing co-registration. Unfortunately, recovering mice from paralysis and mechanical ventilation are challenging. Additionally, paralytics and anesthesia are not practical in human studies, so effective co-registration is also important for human applications.

ANATOMICAL FEATURES

Four dark-bright-dark-bright anatomical layers in the retina and choroid were detected by bSSFP MRI at $45 \times 45 \times 500 \mu\text{m}$. Similar anatomical MRI has been reported in mice using conventional T_1 - and T_2 -weighted spin-echo MRI at $47 \times 47 \times 400 \mu\text{m}$ at 11.7 T (9). Based on the directionality of water diffusion, the outermost of the three retinal layers was assigned as the photoreceptor cells (outer nuclear layer and inner and outer segments), the same as our assignment based on the absence of a hypoxia-induced response. The two inner layers of the retina were assigned to be the nerve fiber/ganglion cell layer, inner plexiform layer, inner nuclear layer, and outer plexiform layer (9), the same as our assignment based on the presence of a hypoxia-induced response.

In rats, three anatomical layers (bright-dark-bright) corresponding to two retinal layers and the choroid were present using T_1 -weighted conventional gradient-echo MRI at $60 \times 60 \times 500 \mu\text{m}$ at 7 T (2). Three similar layers were also observed in the cat retina using T_1 - and T_2 -weighted fast-spin-echo MRI at $50 \times 100 \times 1500 \mu\text{m}$ at 4.7 T (8). In both the rat and cat studies, the inner and outer bright layers were enhanced by intravascular injection of Gadolinium-DTPA (Gd-DTPA), indicating the retinal and choroidal vasculatures. The inner bright layer was assigned as the nerve fiber/ganglion cell layer, inner plexiform layer, and inner nuclear layer. The middle layer unenhanced by Gd-DTPA was assigned as the avascular

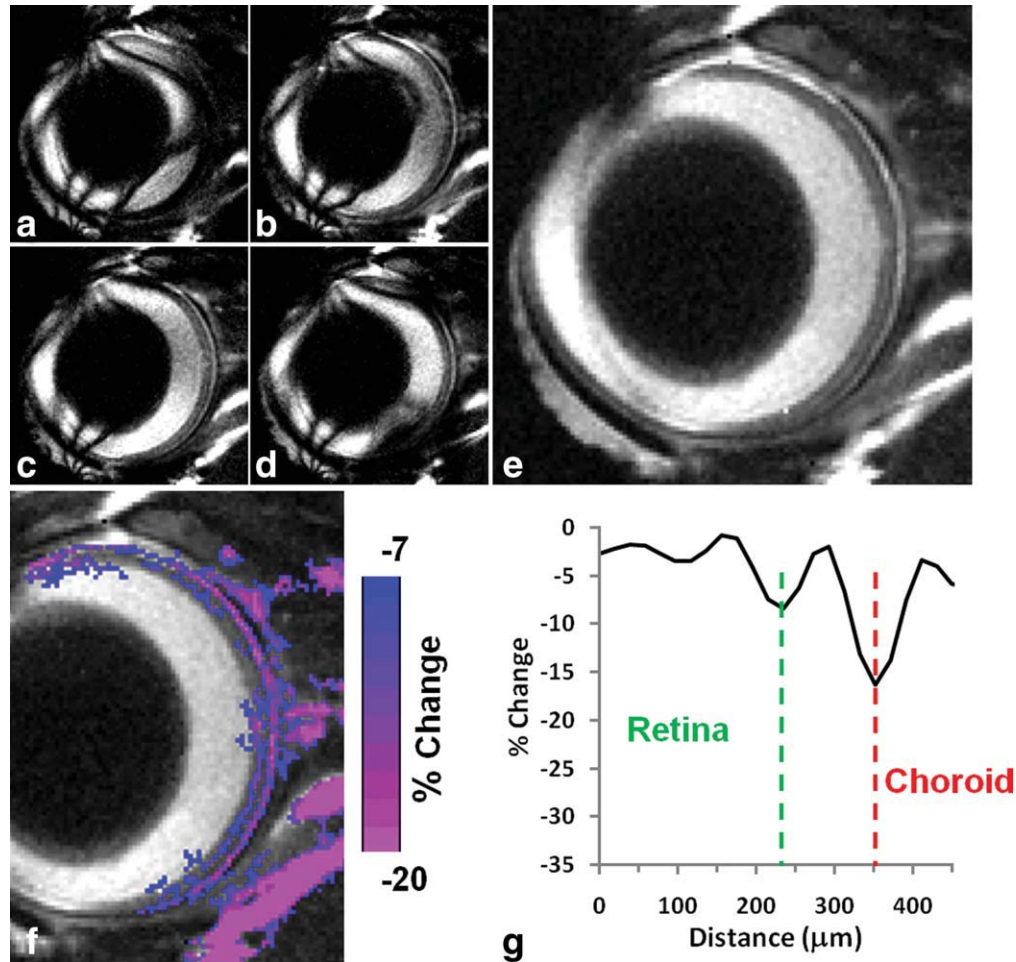


FIG. 4. **a–d**: bSSFP images of the eye with RF phase cycling of 0, 90, 180, and 270°. **e**: The four images are combined to remove banding. **f**: bSSFP fMRI map obtained with RF phase cycling. A 95% confidence interval was used with a %-change threshold of -5 to -100% . **g**: The corresponding %-change profile. [Color figure can be viewed in the online issue, which is available at wileyonlinelibrary.com.]

region (outer nuclear layer and inner and outer segments) (2,8). The discrepancy in the number of layers among these studies could be due to differences in spatial resolution, MRI sequence, and field strength, giving rise to different contrasts. Further studies at higher spatial resolution are needed to unambiguously address these discrepancies.

fMRI OF HYPOXIA IN THE RETINA

The bSSFP signal decrease due to hypoxia was significantly larger in the choroid ($-25.9 \pm 6.4\%$) than in the retinal vascular layer ($-11.6 \pm 2.4\%$). Given the choroidal vessels have a low oxygen extraction fraction compared with the retinal vessels (3,25), the choroid may be less affected by hypoxia, but the opposite was observed. Possible explanations are that the retinal vessels respond to oxygen but choroidal vessels do not (3,5) or the choroid has higher vascular density compared with the inner retina (3,26). Partial volume effect from the vitreous, which has large signal intensity, could also contribute to the smaller response of the retinal vasculature. Previous BOLD fMRI studies of the retina have used diffusion sensitizing gradients (2) or inversion

recovery preparation (14,27) to effectively suppress the strong vitreous signals. Diffusion weighting (2) or inversion recovery (14) could be combined with the SSFP acquisition to avoid possible partial volume effects of the vitreous. The small response of the outer retina in the middle ($-1.57 \pm 1.42\%$, $P = 0.04$) was likely due to partial volume effect with the inner retina and choroid.

The differential retinal and choroidal hypoxia-induced responses are consistent with layer-specific BOLD fMRI of hyperoxia in the rat retina at $90 \times 90 \times 1000 \mu\text{m}$ using diffusion-weighted EPI (2). Layer-specific changes were detected although EPI lacked lamina-specific anatomical layers. Hyperoxia evoked a stronger BOLD response in the choroid compared with the retinal vessels, despite the small arteriovenous oxygen saturation difference in the choroid compared with retinal vessels. Since the diffusion-weighting suppressed potential partial volume effects from the vitreous, the larger choroidal response to hyperoxia was likely due to different responses of retinal and choroidal vessels to oxygen challenge or the larger vascular density of the choroid (3). Retinal vessels strongly vasoconstrict under hyperoxia whereas choroidal vessels do not (3).

CONCLUSIONS

bSSFP of the retina provides anatomical and functional images at high spatiotemporal resolution free of geometric distortion and signal dropout. Passband bSSFP fMRI compares favorably against EPI and conventional imaging. Future studies will include high-resolution fMRI of visual stimulation, other physiological provocations, and applications to mouse retinal diseases, as well as incorporation of bSSFP acquisition to measure layer-specific blood flow in the retina.

REFERENCES

- Cioffi GA, Granstam E, Alm A. Ocular circulation. In: Kaufman PL, Alm A, editors. *Adler's Physiology of the Eye*, 10th ed. St. Louis: Mosby; 2003. pp 747–776.
- Cheng H, Nair G, Walker TA, Kim MK, Pardue MT, Thule PM, Olson DE, Duong TQ. Structural and functional MRI reveals multiple retinal layers. *Proc Natl Acad Sci USA* 2006;103:17525–17530.
- Stone J, Valter K. Roles of oxygen in the stability of photoreceptors. In: Chalupa LM, Williams RW, editors. *Eye, retina, and visual system of the mouse*. Cambridge: MIT Press; 2008. pp 559–572.
- Muir ER, Duong TQ. MRI of retinal and choroidal blood flow with laminar resolution. *NMR Biomed* 2011;24:216–223.
- Riva CE, Cranstoun SD, Grunwald JE, Petrig BL. Choroidal blood flow in the foveal region of the human ocular fundus. *Invest Ophthalmol Vis Sci* 1994;35:4273–4281.
- Pemp B, Schmetterer L. Ocular blood flow in diabetes and age-related macular degeneration. *Can J Ophthalmol* 2008;43:295–301.
- Gilmore ED, Hudson C, Nrusimhadevara RK, Harvey PT, Mandelcorn M, Lam WC, Devenyi RG. Retinal arteriolar diameter, blood velocity, and blood flow response to an isocapnic hyperoxic provocation in early sight-threatening diabetic retinopathy. *Invest Ophthalmol Vis Sci* 2007;48:1744–1750.
- Shen Q, Cheng H, Pardue MT, Chang TF, Nair G, Vo VT, Shonat RD, Duong TQ. Magnetic resonance imaging of tissue and vascular layers in the cat retina. *J Magn Reson Imaging* 2006;23:465–472.
- Chen J, Wang Q, Zhang H, Yang X, Wang J, Berkowitz BA, Wickline SA, Song SK. In vivo quantification of T(1), T(2), and apparent diffusion coefficient in the mouse retina at 11.7T. *Magn Reson Med* 2008;59:731–738.
- Nair G, Shen Q, Duong TQ. Relaxation time constants and apparent diffusion coefficients of rat retina at 7 Tesla. *Int J Imaging Syst Technol* 2010;20:126–130.
- Berkowitz BA, Roberts R, Luan H, Bissig D, Bui BV, Gadianu M, Calkins DJ, Vingrys AJ. Manganese-enhanced MRI studies of alterations of intraretinal ion demand in models of ocular injury. *Invest Ophthalmol Vis Sci* 2007;48:3796–3804.
- Calkins DJ, Horner PJ, Roberts R, Gadianu M, Berkowitz BA. Manganese-enhanced MRI of the DBA/2J mouse model of hereditary glaucoma. *Invest Ophthalmol Vis Sci* 2008;49:5083–5088.
- Duong TQ, Pardue MT, Thule PM, Olson DE, Cheng H, Nair G, Li Y, Kim M, Zhang X, Shen Q. Layer-specific anatomical, physiological and functional MRI of the retina. *NMR Biomed* 2008;21:978–996.
- Duong TQ, Ngan S-C, Ugurbil K, Kim S-G. Functional magnetic resonance imaging of the retina. *Invest Ophthalmol Vis Sci* 2002;43:1176–1181.
- Li Y, Cheng H, Duong TQ. Blood-flow magnetic resonance imaging of the retina. *Neuroimage* 2008;39:1744–1751.
- Li Y, Cheng H, Shen Q, Kim M, Thule PM, Olson DE, Pardue MT, Duong TQ. Blood-flow magnetic resonance imaging of retinal degeneration. *Invest Ophthalmol Vis Sci* 2009;50:1824–1830.
- Zhong K, Leupold J, Hennig J, Speck O. Systematic investigation of balanced steady-state free precession for functional MRI in the human visual cortex at 3 Tesla. *Magn Reson Med* 2007;57:67–73.
- Miller KL, Smith SM, Jezzard P, Wiggins GC, Wiggins CJ. Signal and noise characteristics of SSFP FMRI: a comparison with GRE at multiple field strengths. *Neuroimage* 2007;37:1227–1236.
- Lee JH, Dumoulin SO, Saritas EU, Glover GH, Wandell BA, Nishimura DG, Pauly JM. Full-brain coverage and high-resolution imaging capabilities of passband b-SSFP fMRI at 3T. *Magn Reson Med* 2008;59:1099–1110.
- Miller KL, Jezzard P. Modeling SSFP functional MRI contrast in the brain. *Magn Reson Med* 2008;60:661–673.
- Gruetter R. Automatic, localized in vivo adjustment of all first- and second-order shim coils. *Magn Reson Med* 1993;29:804–811.
- Elliot AM, Bernstein MA, Ward HA, Lane J, Witte RJ. Nonlinear averaging reconstruction method for phase-cycle SSFP. *Magn Reson Imaging* 2007;25:359–364.
- Jung KJ. Synthesis methods of multiple phase-cycled SSFP images to reduce the band artifact and noise more reliably. *Magn Reson Imaging* 2010;28:103–118.
- Duong TQ, Muir ER. Magnetic resonance imaging of the retina. *Jpn J Ophthalmol* 2009;53:352–367.
- Bill A, Sperber GO. Aspects of oxygen and glucose consumption in the retina: effects of high intraocular pressure and light. *Exp Ophthalmol* 1990;228:124–127.
- Nair G, Tanaka Y, Kim M, Olson DE, Thule PM, Pardue MT, Duong TQ. MRI reveals differential regulation of retinal and choroidal blood volumes in rat retina. *Neuroimage* 2011;54:1063–1069.
- De La Garza BH, Muir ER, Li G, Shih YY, Duong TQ. Blood oxygenation level-dependent (BOLD) functional MRI of visual stimulation in the rat retina at 11.7 T. *NMR Biomed* 2011;24:188–193.